

Injectivity decline by nanoparticles transport in high permeable rock

Fadili, Ali; Murtaza, Ali; Zitha, Pacelli

DOI

[10.1016/j.petrol.2022.110121](https://doi.org/10.1016/j.petrol.2022.110121)

Publication date

2022

Document Version

Final published version

Published in

Journal of Petroleum Science and Engineering

Citation (APA)

Fadili, A., Murtaza, A., & Zitha, P. (2022). Injectivity decline by nanoparticles transport in high permeable rock. *Journal of Petroleum Science and Engineering*, 211, Article 110121. <https://doi.org/10.1016/j.petrol.2022.110121>

Important note

To cite this publication, please use the final published version (if applicable). Please check the document version above.

Copyright

Other than for strictly personal use, it is not permitted to download, forward or distribute the text or part of it, without the consent of the author(s) and/or copyright holder(s), unless the work is under an open content license such as Creative Commons.

Takedown policy

Please contact us and provide details if you believe this document breaches copyrights. We will remove access to the work immediately and investigate your claim.

Green Open Access added to TU Delft Institutional Repository

'You share, we take care!' - Taverne project

<https://www.openaccess.nl/en/you-share-we-take-care>

Otherwise as indicated in the copyright section: the publisher is the copyright holder of this work and the author uses the Dutch legislation to make this work public.



Injectivity decline by nanoparticles transport in high permeable rock

Ali Fadili^{a,*}, Ali Murtaza^b, Pacelli Zitha^b

^a Shell Global Solutions International B.V., The Hague, Netherlands

^b Delft University of Technology, Netherlands

ARTICLE INFO

Keywords:

Nanoparticle transport
Ultrafiltration
Injectivity decline
Formation damage
Deep bed filtration
Numerical modelling

ABSTRACT

Water injection into the subsurface, inherent in improved hydrocarbon recovery and extraction of geothermal energy, often suffers from injectivity decline, even when water carries only nano-sized particles at low concentrations. This study investigates the propagation of such nano-sized particles experimentally and by modelling. Water with dispersed silica nanoparticles of about 140 nm diameter was used as a proxy to ultra-filtered water. Dispersion of the nanoparticles in brine is investigated by varying their concentration, the brine composition, salinity, pH and the presence of iron ions. The measured apparent hydrodynamic size and zeta potential indicate that nanoparticles remain dispersed with the expected size only for salinity below 3000 ppm with pH ranges 6.5 to 8.5. For higher salinity or pH outside that range or presence of iron ions, agglomeration becomes strong. Core flood experiments are conducted on high permeability Bentheimer sandstone, and the transport and retention of nanoparticles in the cores was analysed using multiple pressures measured along the core and by influent/effluent analysis. Core flood results show that stable injectivity can be reached with a good propagation of the nanoparticles through the permeable core with no external filter cake formation, provided the pH and salinity of the injected fluid are kept within the dispersion range and free of iron ions. However, injectivity decline still occurs in three characteristic stages well captured by our mechanistic model used to match the data. This study will contribute to better understanding of the transport dynamics of nanoparticles in the subsurface and to better modelling prediction and assessment of technologies where transport of nanoparticles is key.

1. Introduction

Water injection into the subsurface is critical to many industrial applications including hydrocarbon recovery (Willhite, 1986; Veil and Clark, 2011), geothermal (Watson, 2017), and groundwater resource management, to name a few. Millions of cubic meters of water is (re)-injected daily into the subsurface in these applications. Therefore, addressing the injection performance challenges is paramount to ensure a sustained water injection level.

The porous structure acts as a natural filter for suspended particles, which get captured creating an internal “damage”, which eventually may develop into an internal filter cake (IFC) as depicted in Fig. 1 right. Larger particles are unlikely to penetrate the porous medium and deposit at the injection face, eventually forming an external filter cake (EFC) (Clark et al., 2010; Nabzar et al., 1997; Bedrikovetsky et al., 2001; Civan, 2007; De Zwart, 2007; Vilks et al., 1991; Elimelech et al., 2013; Abrams, 1977; Eylander, 1988; Khatib, 1994; Liu and Civan, 1996; Sharma et al., 2000; Altoe F et al., 2004; Yi et al., 2009; Hofsaess and

Kleinitz, 2003; Al-Abduwani et al., 2004; Alaskar et al., 2012; Al-Abduwani, 2005; Costier et al., 2009).

Filter cakes cause a drastic reduction in injectivity (Barkman and Davidson, 1972; Al-Abduwani et al., 2004; Murtaza, 2017). To reduce the formation of these filter cakes and comply with the environmental regulations, water is extensively treated and filtered prior to injection. Typical filtration practices (micro-filtration) can remove dispersed particles down to micron-sized, typically 2–5 μm (Bedrikovetsky et al., 2001; Al-Abduwani, 2005; Kalantariasl, 2015; Bennion et al., 2001). New filtration technology, such as ultra-filtration, enables the removal of particles down to nano-size. Most of the published work on injection decline uses particles in micron range (typically 1 to 5 μm) and has clearly demonstrated a systematic formation of an IFC followed by EFC or a direct EFC build-up (Civan, 2007; Eylander, 1988; Liu and Civan, 1996; Hofsaess and Kleinitz, 2003; Alaskar et al., 2012; Al-Abduwani, 2005; Buret et al., 2010; Ryan and Elimelech, 1996). Empirical rules for predicting injectivity performance, such as the “1/3–1/7” rule, based on the pore size distribution and particle size (Elimelech et al., 2013), do

* Corresponding author.

E-mail address: Ali.Fadili@shell.com (A. Fadili).

<https://doi.org/10.1016/j.petrol.2022.110121>

Received 17 September 2021; Received in revised form 10 December 2021; Accepted 4 January 2022

Available online 8 January 2022

0920-4105/© 2022 Elsevier B.V. All rights reserved.

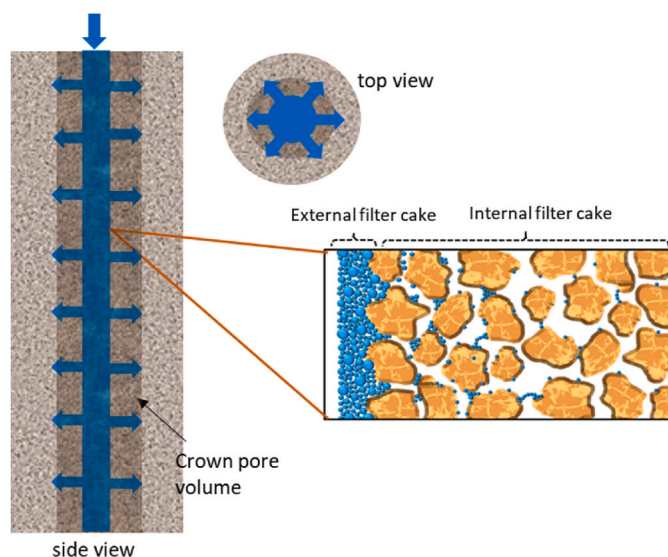


Fig. 1. Schematic of an injection well with a crown region (darker) where high volume of the water rich particles first goes through. On the right, zoom-in illustrating the particle accumulation leading to an internal and external filter cake.

not consider the effects of surface forces that increase significantly as particles size reduces. This particular rule of thumb basically states that particles below $1/7$ of the pore diameter will flow through with no damage. We will show that although we have a well separated nano size distribution and pore size distribution, therefore being well below the $1/7$ bound, nanoparticle trapping occurs and leads to injectivity decline.

For nanosized particles injection in subsurface formation, most of the published work was aimed at demonstrating the benefits of nanoparticles in enhanced oil recovery (EOR) either on their own or in combination with other EOR technologies (Dordzie and Dejam, 2021). The experimental work is based on very limited injection volume (at most 10 PVs). Those limited injection volumes did not show injectivity issues as per (Olayiwola, 1151). However, the vicinity of an injection well, e.g., a crown of a few centimetres as illustrated in Fig. 1, will see a significant amount of water rich particles (equivalent to thousands/millions of PV) which will eventually accumulate, reduce the pore space and permeability around the well. It is this realistic scenario which has been investigated in this work by conducting core flood experiments using very high injection volumes ($>40\,000$ PV). The risk caused by potential corrosion products in the flow lines are also illustrated using iron ions. Our review work on nanoparticles showed a lack of systematic characterization of surface forces on the nanoparticle dispersions (Al-Abduwani et al., 2004; Ives, 1969; Kottsova et al., 2021). These surface forces appear to be very restrictive in the salinity level and pH range of brines and in terms of potential corrosion by-products content such as iron ions.

Therefore, the primary objective of this study is to gain a better understanding of the impact of those factors on nanoparticle dispersions and on their propagation in natural sandstones. Hence, a systematic analysis of the flow of brine containing nanoparticles, as a proxy to the ultra-filtered injection water, in Bentheimer sandstone cores was performed. Based on the core flood results, a mechanistic transport model is developed and solved numerically to aid the interpretation of the experiments and test the hypotheses underlying this work.

The rest of the paper is organized as follows. First, we provide the details of the material and methods to gather our experimental data. This contains component characterizations, details of the core flood protocol and testing. Then, the experimental results are discussed in detail with the mechanistic transport model based on obtained results. Last, some conclusions and potential follow-up suggestions are given.

2. Material and methods

Our experimental approach can be described with the aid of the ternary diagram shown in Fig. 2. Each element at the vertices (porous media, brine, nanoparticles) of the triangle was characterized separately, then binary systems represented by the edges were examined in detail. Finally, the ternary system combining all three elements at the vertices of the triangle was thoroughly studied in the core flood tests. The effect of physical parameters (nanoparticle concentration, salinity, composition, pH, permeability, corrosion) was tested by varying only one of them at a time.

2.1. Porous media

Bentheimer sandstone was selected for our core flood experiments. The rock samples have good lateral continuity and homogeneity (Coradin et al., 2004). Table 1 shows the mineral composition obtained by XRD/XRF (X-ray diffraction/X-ray Fluorescence) analysis (Costier et al., 2009).

Porosity and pore size distribution were determined by Mercury Intrusion Porosimetry (MIP) measurements on a rock sample taken from the same block as the core samples used in the core floods (Fig. 4). Again, our data compares well to previously published data as per Table 2.

Cylindrical cores having 4.0 cm diameter were drilled out of a large Bentheimer sandstone's block and then cut to the desired length. The core plugs were then dried in an oven at a temperature of $60\text{ }^{\circ}\text{C}$ for 48 h to remove water content. They were then placed in the moulds and coated with self-hardening glue (Araldite CW2215 with a hardener HY5160). Excess glue was machined afterwards so that the core plug fits in the core holder precisely. Three holes were drilled for pressure ports along the core at 21 mm, 53 mm and 85 mm from the inlet as illustrated in Fig. 3. Core plugs were further dried in the oven for 24 h at $30\text{ }^{\circ}\text{C}$.

2.2. Nanoparticles characterization

Silica (SiO_2) nanoparticles were used in all experiments because of their availability in nano-size, spherical shape and potential negative surface charge to minimize retention. Fig. 4 shows TEM (Transmission Electron Microscope) images of two batches of the silica nanoparticles provided by the supplier. These images confirm the spherical shape as well as indicate a tendency for agglomeration.

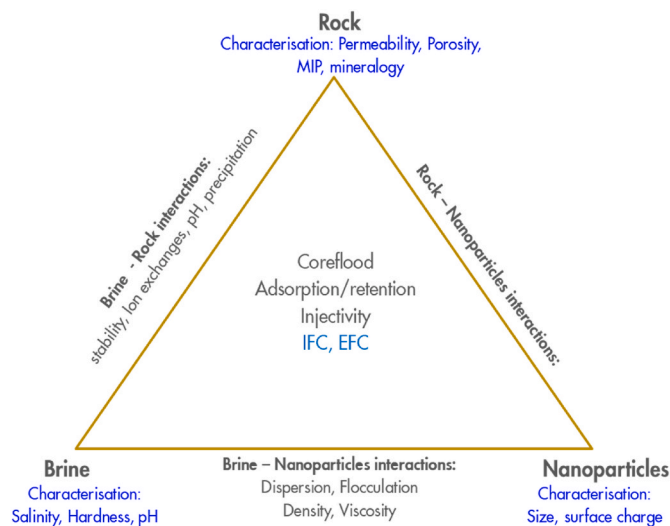


Fig. 2. Schematic of the ternary system with an indication of the type of component characterization, binary interactions, and eventually ternary interactions when all components are put together in a core flood.

Table 1
Mineral composition of Bentheimer sandstone from this study and literature.

Study	Quartz	Clay	Feldspar	Other
	wt %	wt %	wt %	wt %
This study	92.0	2.80	4.50	0.70
Peksa et al. (2015) (Coradin et al., 2004)	91.7	2.68	4.86	0.76
Maloney et al. (1990) (Peksa et al., 2015)	97.5	0.50	2.00	Traces
Van Baaren et al. (1990) (Maloney et al., 1990)	95.0	3.00	2.00	–

Table 2
Porosity and pore diameter results for Bentheimer sandstone from this study and literature.

Study	Pore Size	Porosity		
	Avg. Pore diameter [mm]	Avg. from MIP	Avg. from imaging methods ^a	Avg. from laboratory methods ^b
This study	0.013	0.234	–	–
Peksa et al. (2015) (Coradin et al., 2004)	0.014	–	0.254	0.248
Halisch et al. (2013) (Van Baaren et al., 1990)	–	0.215	–	–
Dautriat et al. (2009) (Halisch et al., 2013)	–	0.240	–	–
Klov (2000) (Dautriat et al., 2009)	–	0.220	0.215	–

^a Average from imaging methods based on Image Analysis, Micro and Medical CT Scanning.

^b Average from laboratory methods based on Ultra Pycnometer and Gravitometric methods.

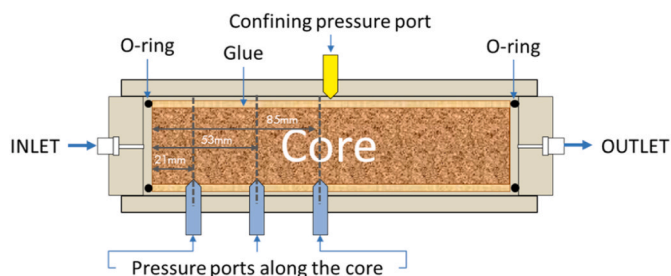


Fig. 3. Details of the core holder and core plug set-up showing the location of the different pressure measurement points along the core, and confining pressure (in yellow). (For interpretation of the references to colour in this figure legend, the reader is referred to the Web version of this article.)

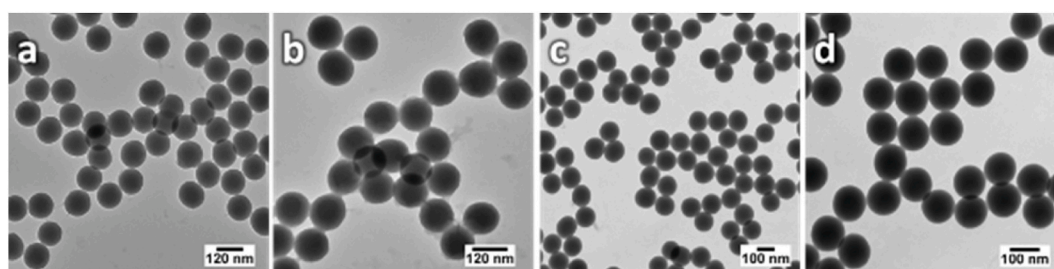


Fig. 4. Transmission Electron Microscope (TEM) images of two batches of the silica nanoparticles provided by nanoComposix (JEOL 1010): batch 1 - a) & b); batch 2: c) & d). Note their tendency to agglomerate. Scale on the picture shows individual nanoparticle size of about 100–120 nm (picture b).

Zetasizer Nano-ZS (Malvern instruments) apparatus that uses the Dynamic Light Scattering (DLS) principle to determine the hydrodynamic size and zeta potential, was used to confirm the size of nanoparticles. When milliQ brine is used, our measurements confirmed the supplier specifications as shown in Table 3.

Nanoparticle size distribution along with the pore size distribution of the Bentheimer core plugs shows a clear separation between the two distributions as shown in Fig. 5. The difference in the average (peaks) size between the nanoparticles and pore size is a couple of order of magnitude. Based on these distribution sizes, applying the “1/3–1/7” rule (Elimelech et al., 2013) would predict no plugging as nanoparticles would flow through the porous space easily. The experiments reported in this study will show that this is not the case.

To define a reference for the post-mortem analysis of the core flood, SEM images of the dried nanoparticles were also taken as shown in Fig. 6. As expected, the dried nanoparticles form aggregates.

2.3. Nanoparticle concentration measurement

Silica concentrations in influent and effluent were measured by the silicomolybdate method (Lawson et al., 2016; Coradin et al., 2004). In this method, first, a molybdate reagent pillow is added to a 10 ml sample containing silica and swirled until it dissolves. Then an acid reagent pillow is added and swirled until it dissolves as well. Silica reacts with molybdate ions under acidic conditions to form yellow coloured Silicomolybdic acid complexes ($H_4[SiO_4.Mo_{12}O_{36}].xH_2O$). The sample is given 10 min reaction time. At this point, the suspension will turn yellow if silica is present. The sample is then placed in a spectrophotometer to measure absorbance. The silica concentration is then determined using a calibration curve.

2.4. Brine and nanoparticle suspension

Brines with different salt concentrations and pHs were prepared and then filtered through a 0.45 μm Nuclepore™ filter. To mimic ultra-filtered water, different concentrations of silica nanoparticles were added to these synthetic brine samples. The apparent size and zeta potential of the nanoparticles were then measured using Zetasizer. This screening analysis was used to select the brine salinity and pH for the core floods. For application purposes, synthetic seawater composition was chosen as the brine for the core floods. Bulk tests were performed to determine the parameter's (pH and salinity) range where nanoparticles remained dispersed in suspension so that their apparent size is about 140 nm with a negative zeta potential (see section 3.1).

2.5. Core flood set-up

The core flood experimental setup is depicted in Fig. 7. Two types of pumps were used for the injection: either an ISCO 500D-Series, dual syringe pump of 0.5% accuracy or a Quizix-QX pump of 0.1% accuracy. Differential pressure transducers of ± 40 Bar and ± 3 Bar rating were used to measure pressures along the core. Inlet and outlet pressures were

Table 3
Specifications of Silica nanoparticles as provided by nanoComposix and measured in this study.

Batch No.	Supplier Datasheet						Measured in this study			
	Solvent		Shape	Size		Zeta Ptnl. [mV]	Solvent		Size	Zeta Ptnl. [mV]
	Type	pH	TEM	TEM [d.nm]	DLS [d.nm]		Type	pH	DLS [d.nm]	
1	Milli-Q water	9.1	Spherical	119 ± 6	148.4	-63.3	Milli-Q water	8.3	144.8	-48.8
2	Milli-Q water	9.5	Spherical	119 ± 6	138.0	-51.0	Milli-Q water	8.1	140.2	-43.7

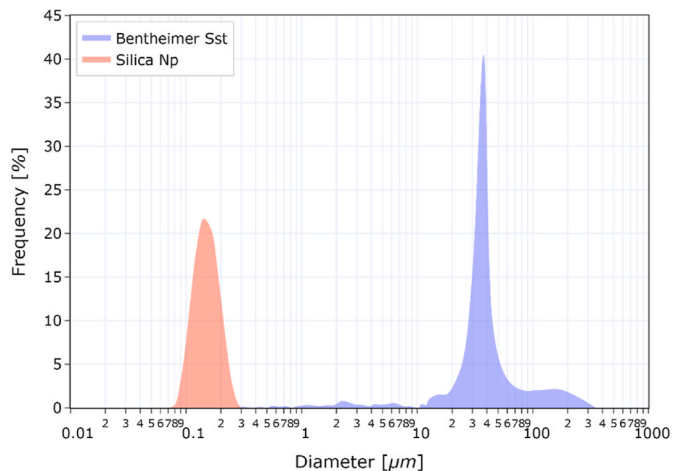


Fig. 5. Comparison of Silica nanoparticle size distribution and Bentheimer sandstone pore size distribution.

recorded using pressure sensors of ± 50 Bar rating. All pressure and differential pressure sensors were calibrated prior to experiments and had an offset of ± 0.001 Bar and ± 0.01 Bar respectively about the set point. Flow lines were made of plastic tubing with a pressure rating of 38 Bar. Core plug holder was made of Poly Ether Ketone (PEEK). Once the core plug was mounted, the experimental setup could withstand pressure up to 38 Bar and temperature up to 70 °C.

2.6. Core flood procedure

Before starting experiments, the cumulative volume of all flow lines, connections and valves was measured to estimate the time a water droplet would take to go through the setup. This time was then used to get representative influent and effluent sampling. All experiments were conducted at a temperature of 24 ± 3 °C with a back pressure of 2 ± 1 Bar and confining pressure of 25 ± 1 Bar. The following diagram summarises the protocol used for the corefloods.

3. Results and discussion

In this section, we discuss the characterization of the nanoparticles in suspension (section 3.1), present the evidence of the nanoparticle retention (section 3.2) and examine the sensitivity of such retention to important physical parameters.

3.1. Effect of salinity and pH on nanoparticle dispersion

To study the effect of salinity on nanoparticle dispersion, synthetic seawater along with simpler composition brine (KCl, NaCl) samples with pH around 7 were prepared and analysed using Zetasizer. We observed that the apparent size increases with an increase in salt and/or nanoparticle concentration as shown in Table 4. Based on this screening, the highest salinity for which nanoparticles remain dispersed needed to be below 3000 ppm. Hence, a $20 \times$ diluted synthetic Seawater with a salinity of 1500 ppm was selected for further characterization and the core floods. Details of synthetic seawater composition can be found in (Murtaza, 2017).

Once the salinity was fixed, four sets containing five samples each of diluted synthetic seawater suspensions were prepared by changing the nanoparticle concentration: 500 ppm, 250 ppm, 100 ppm and 10 ppm. In each set, pH was varied by adding drops of 1 M HCl and 1 M NaOH solutions. As shown in Fig. 8, pH value within 6.5–8.5 keeps the size of the dispersed nanoparticles within the \varnothing 140 nm (Fig. 8 left). These tests clearly show the importance of the surface charges whereby at a higher magnitude of zeta potential (Fig. 8 right), repulsive forces between particles are strong enough to prevent aggregation. Some variation in size can be seen for different nanoparticles concentrations, but the overall behaviour remains the same. Similar tests were considered to investigate the rock surface behaviour in terms of surface charge to have some indications on the potential of nanoparticles to adsorb on the rock surface, but unfortunately, the results were not reproducible and were therefore disregarded in this study. Based on this characterization step, the pH of suspension was kept between 6.5 and 8.5 to have dispersion of nanoparticles of 140 nm for the core floods.

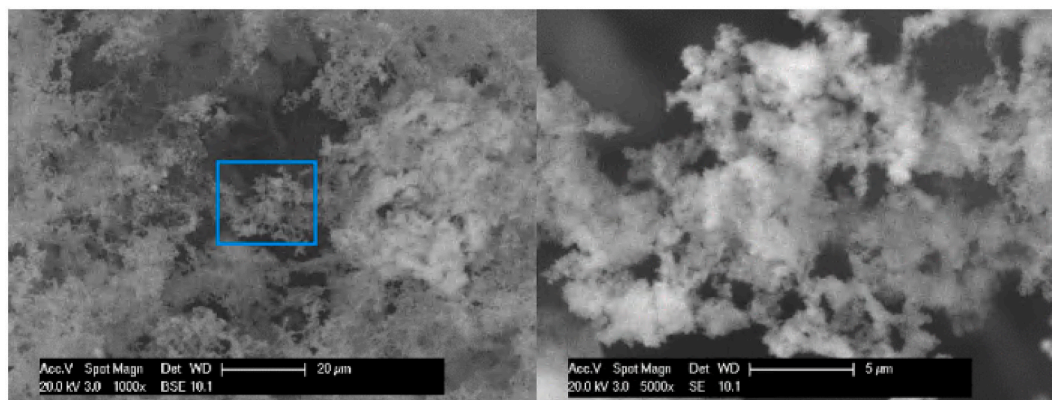


Fig. 6. SEM pictures of the silica nanoparticles, with a higher resolution (5micron) on the right picture.

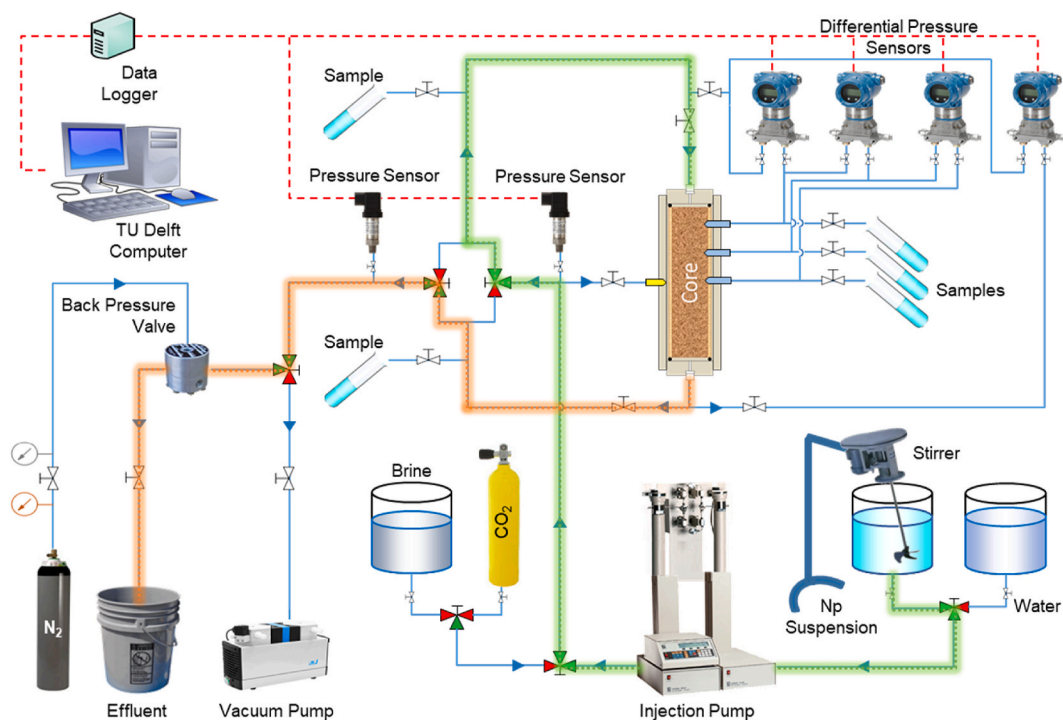


Fig. 7. Experimental setup diagram. The injection path is highlighted in green, and the effluent part is highlighted in orange. Note the stirrer in the nanoparticle (np) container to prevent potential np settling. (For interpretation of the references to colour in this figure legend, the reader is referred to the Web version of this article.)

3.2. Core flood tests

Seven core flood (CF) experiments, labelled CF-1 through CF-7, were performed, whereby different flow conditions were tested (flow rate, suspension concentration, pH and iron ions). Flow rates were based on realistic well leak-off rates, whereby for a well injection rate of about 10,000 bbl/day, with an effective completion (open-hole) height of 15 m and radius of 0.1 m, the average flux will be about 11.6 ml/cm²/min, which is in-line with what we used in our experiments. Hence, for most of the core floods, the injection rate was set at 141 ml/min, and the pressure build-up was monitored. Core sample data and injection parameters are summarized in Table 5.

In all the experiments, the reference permeability k_0 was first measured after injecting several pore volumes of brine alone without nanoparticles. This was done to ensure that permeability does not change any further due to brine-rock only interaction. It was observed that permeability reduction with brine alone was between 1.5% and 10% until stabilizing to its reference value k_0 as shown in Table 6. This reduction could be due to fines migration and/or clay swelling, which would be consistent with the XRD analysis of Table 1.

3.2.1. Evidence of nanoparticles retention

3.2.1.1. Pressure build-up. Despite the optimum salinity and pH conditions along with a clear separation in the probability density functions for the nanoparticles and pore radii (see Fig. 5), increase in pressure drop was observed in all experiments indicating injectivity decline. Fig. 9 shows the typical pressure profile along the core (left) with the evolution of pressure drop over the core and corresponding permeability ratios (right) for CF-2. All the core floods show similar behaviour in terms of pressure profiles, with the highest gradient in the first section near the injection face (Fig. 9, left). A gradual increase in pressure drop occurs until a stabilization around 30000 PV (Fig. 9 right, red curve). When this increase in pressure drop is interpreted in terms of permeability decline (Fig. 9 right, blue curve), this translates into more than half of the initial permeability being lost before stabilization at about

$k/k_0 \sim 0.47$. CF-2a corresponds to flow reversal and is discussed in section 3.2.2.2.

3.2.1.2. Effluent nanoparticle concentrations. Fig. 10 displays the normalized concentration of nanoparticles measured as described in Section 2.3, along with the cumulative mass of nanoparticles retained in the porous medium. Looking at the effluent concentrations, for the three experiments CF-2, 3 and 4, we observed that: (1) the nanoparticles concentration in the effluent jumps from 0 to 0.8–0.9 of the injected value in the first few PVs, which demonstrates a very good propagation of the nanoparticles with limited retention; (2) subsequently the concentration continues to increase gently until it reaches unity. For instance, for CF-4 (with 100 ppm np conc.) the cumulative mass of retained nanoparticles increases almost linearly until about 2.5×10^4 PV before reaching a plateau showing that no extra retention occurs. This corresponds to about 113 g of injected nanoparticles. The cumulative mass of retained nanoparticles of about 23 g at the plateau, corresponds to $\sim 20\%$ of the mass of injected nanoparticles. This represents nanoparticles bulk volume of about 23% of the total core PV since the density of particles is about 2.2 g/cm³. The two other core floods CF-2 (100 ppm) and CF-3 (50 ppm) exhibit the same behaviour although with a higher number of pore volumes injected. The fact that it takes over ten thousand PV for the normalized nanoparticles concentration to reach unity, and for the mass of retained nanoparticles to level off to a plateau, is a clear evidence that nanoparticles are retained in the porous medium.

3.2.1.3. Core flood post-mortem with SEM analysis. The retention of nanoparticles in the porous medium was further confirmed by the post-mortem analysis of a core sample after the core flood. This analysis was only done for experiment CF-2 due to limited access of the SEM. The core was broken into half along the flow direction to avoid water flushing if the core was to cut with a saw. The freshly broken core surface was imaged using SEM to visualize the shape, size, arrangement and location of the nanoparticles within the pore network. Fig. 11 shows the SEM images of a section of the core, where a chain of nanoparticles can be seen at the entrance of a pore. Energy Dispersive Spectroscopy (EDS)

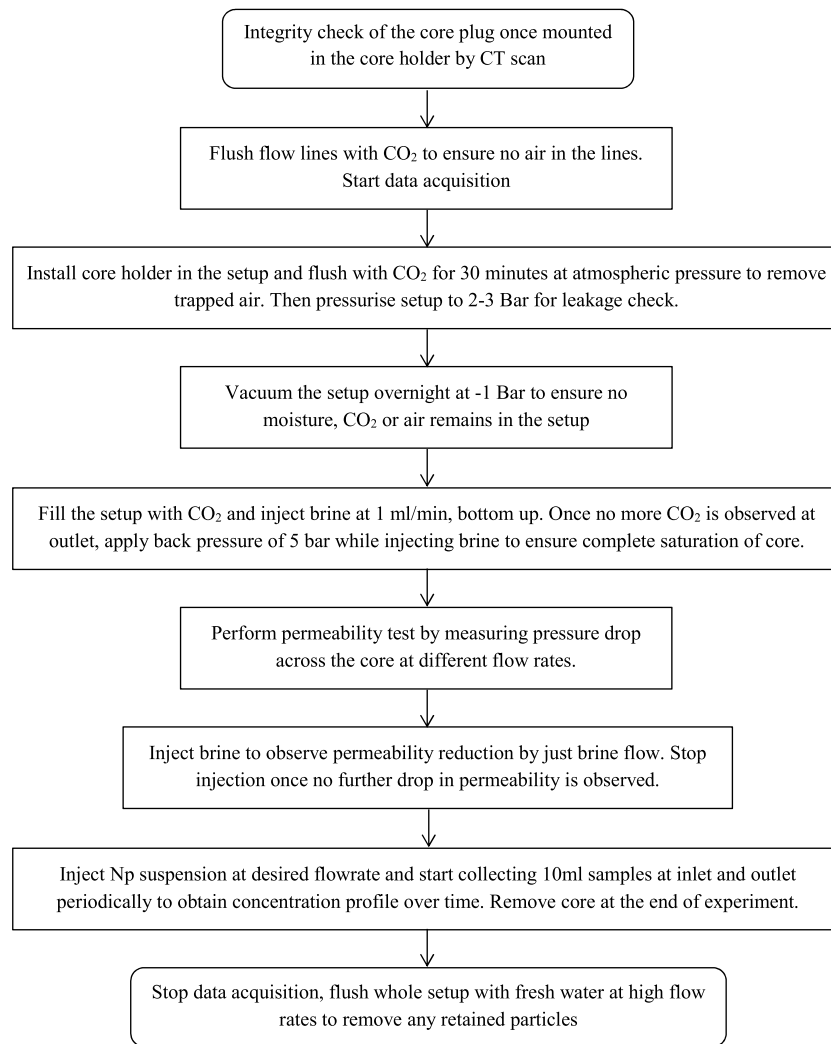


Table 4
Size and zeta potential analysis of silica nanoparticles in different brines.

Sample No.	Brine	Salt Conc.	Particle Conc.	pH	Avg. Particle Size	Avg. Zeta Ptnl.
		ppm	ppm		d.nm	mV
SW-1	Synthetic Seawater	33123	10	7.8	671.5	–
SW-2	Synthetic Seawater	33123	100	8.7	1160.0	–
DSW-1	Diluted Seawater	3312	10	8.0	145.4	–21.3
DSW-2	Diluted Seawater	3312	100	8.9	136.3	–23.7
SN-1	NaNO ₃	850	100	7.1	135.9	–37.5
PC-1	KCl	30000	100	7.2	1602.0	–
SC-1	NaCl	10000	100	7.5	954.3	–17.6
SC-2	NaCl	10000	100	9.4	110.8	–28.2

was used to confirm that those chains were indeed made of silica nanoparticles. This also shows that despite bulk optimal conditions to keep nanoparticles dispersed, agglomeration may still occur inside the core because of local variations of the fluid properties (e.g., pH).

3.2.1.4. Mechanistic concept for nanoparticle retention. Based on the aforementioned observations, a mechanistic model for the retention of

nanoparticles under the conditions of this study is proposed as illustrated in Fig. 12. For flow of diluted suspension of nanoparticles mimicking ultra-filtered water through natural rock, the injectivity declines in three main stages: a) static deposition whereby nanoparticles adsorb to the rock and reduce the pore space available for flow; b) plugging stage whereby bridging builds up and reduces further the major flow paths focusing the flow in reduced areas and c) entrainment stage where increased velocity in those reduced flow paths starts to balance the nanoparticle retention. This mechanistic model will be tested later (section 3.2.2 and modelling and numerical simulations section 3.3).

3.2.2. Sensitivity analysis

We now proceed with the analysis of the sensitivity of the core floods to the main physical parameters, i.e., duration of core floods, nanoparticle concentration, permeability, pH and iron ions. This provides a more detailed insight into the retention process and serves as a basis to support the conceptual retention model. The experiments conducted were grouped into three sets as follows:

1. CF-1 to CF-4: $6.5 \leq \text{pH} \leq 8.5$. pH is kept in the optimal range (see section 3.1). This set tests the size of injected volumes, nanoparticles concentration effect and permeability/reproducibility of the results.

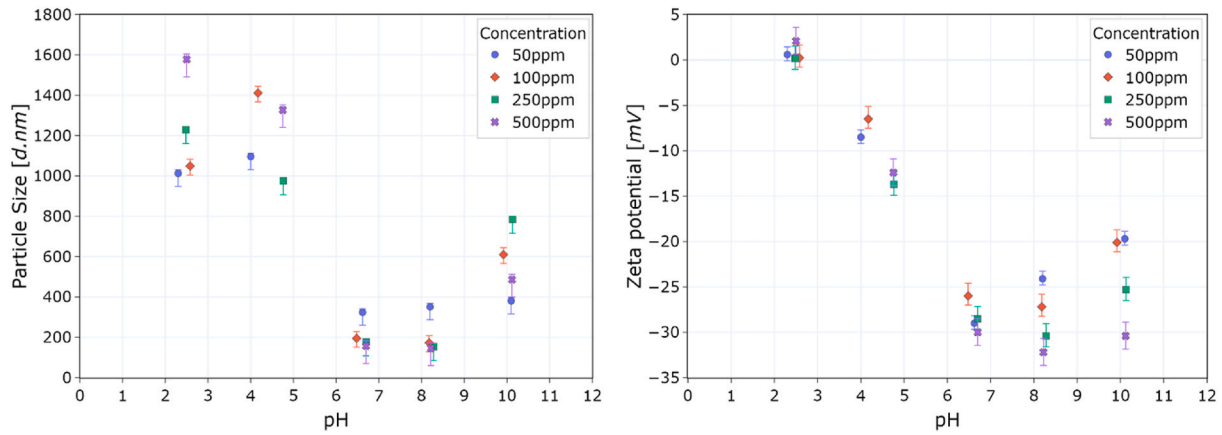


Fig. 8. Particle size (left) and zeta potentials (right) versus pH, measured in 20 times diluted seawater (1500 ppm) showing the range of pH (6.5–8.5) for which the size of the nanoparticles is the smallest.

Table 5
Core sample and flow parameters along with the duration of each experiment.

Exp. No.	Length cm	Diameter cm	X-Sec. Area cm ²	Pore Volume cm ³	Initial brine Perm Darcy	pH	Np Conc. ppm	Injection Rate cm ³ /min	Total PV Injected PV	Duration hours
CF-1	17.05	3.85	11.64	45.65	2.85 ± 0.15	7.2	50	47	2188	35.4
CF-2	17.00	3.80	11.34	44.35	2.71 ± 0.10	7.1	100	141	43142	226.2
CF-3	16.95	3.85	11.61	45.27	3.05 ± 0.10	7.4	50	141	38543	206.2
CF-4	16.95	3.85	11.61	45.27	3.30 ± 0.10	7.3	100	141	38639	206.7
CF-5	17.00	3.85	11.61	45.40	2.92 ± 0.10	9.6	100	141	5188	27.8
CF-6	17.00	3.85	11.61	45.40	3.08 ± 0.10	4.0	100	141	6114	32.8
CF-7	10.54	3.85	11.64	28.18	3.24 ± 0.23	6.8	50	47	1790	17.9

Table 6
Permeability reduction (%) by brine alone for each experiment.

Exp. No.	Pore Volume cm ³	pH	Injection Rate cm ³ /min	Brine Injected PV	Initial brine Permeability Darcy	Reference Perm. (k ₀) Darcy	Permeability Reduction with brine only %
CF-1	45.65	7.2	47	1073	2.85	2.59	9.1
CF-2	44.35	7.1	141	4548	2.71	2.62	3.3
CF-3	45.27	7.4	141	834	3.05	2.97	2.5
CF-4	45.27	7.3	141	3089	3.30	3.21	2.6
CF-5	45.40	9.6	141	4593	2.92	2.87	1.7
CF-6	45.40	4.0	141	1061	3.08	2.75	10.0
CF-7	28.18	6.8	47	-	3.24	-	-

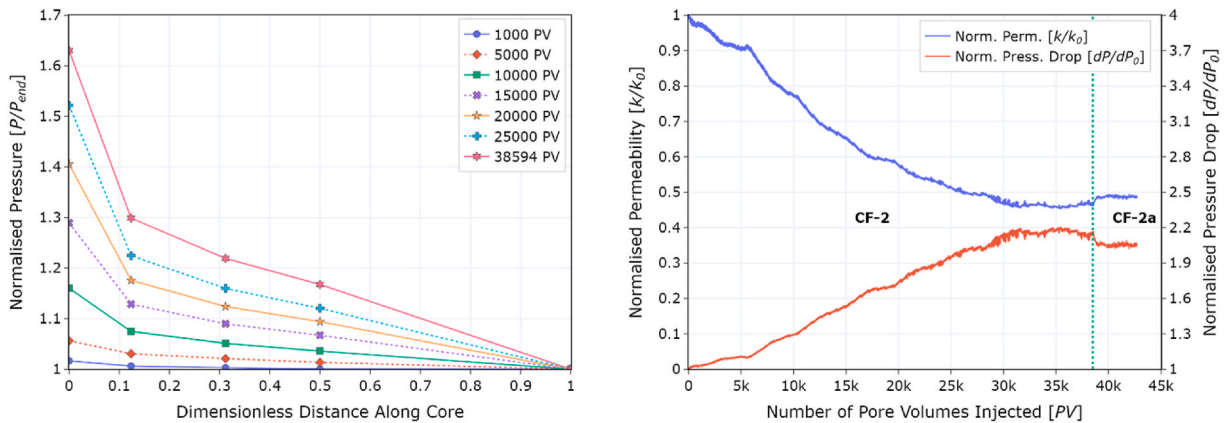


Fig. 9. Pressure profile along the core length (left) and evolution of pressure drop of the core and permeability ratios for CF-2 (right). CF-2a corresponds to flow reversal testing.

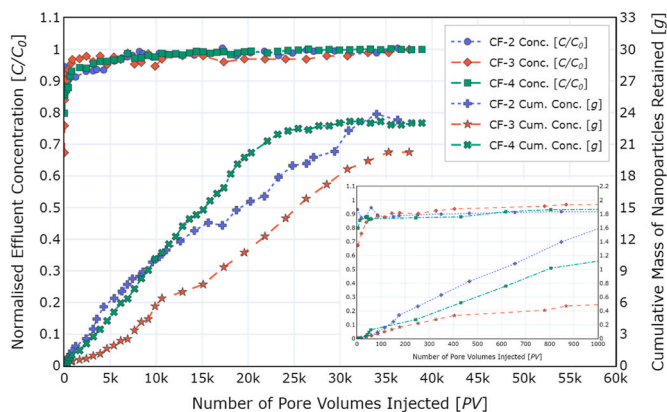


Fig. 10. Normalized concentration and mass of nanoparticles retained in the core in the effluents versus the number of PV injected. Inset: zoom on the first 1000 PV. Normalized effluents concentration reach 80%–90% in the first PVs before a gentle (linear) increase towards unity.

2. CF-5 and CF-6: pH ~9.6 and pH ~4.0. In these experiments, the effect of aggregation due to pH outside the optimal range is tested in the core floods.
3. CF-7 tests the impact of iron ions ($Fe^{2+/3+}$) in presence of a fracture along the core.

In all cases, the reference brine permeability k_0 was first determined as per Table 6. For ease of comparison, we kept the scale in the pressure plots the same for CF-1 to CF-4. Table 7 summarises the results obtained for injectivity decline for all experiments.

3.2.2.1. Duration of the core floods. Experiment CF-1 aimed at setting a reference for the other core floods and test some of the parameters reported in the literature. The nanoparticle concentration was 50 ppm. The duration of this experiment was in line with core flood durations reported in literature i.e., usually from a few hundred pore volumes to thousand pore volumes (Clark et al., 2010; Alaskar et al., 2012; Civan, 2015). In terms of behaviour, the pressure drop is happening mainly near the inlet (Fig. 13, left), which is in line with the fact that in terms of equivalent PV, the first section of the core sees a significantly higher

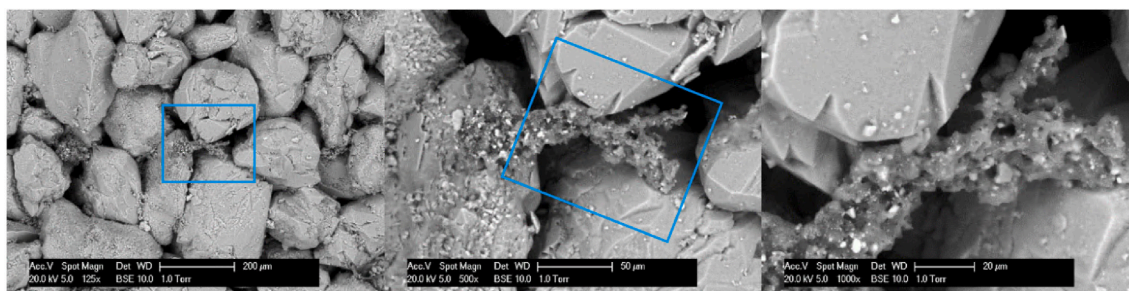


Fig. 11. SEM images in one of the sections of the sandstone core showing small chains of nanoparticles at the entrance of a pore. The higher resolution left has a scale of 20micron.

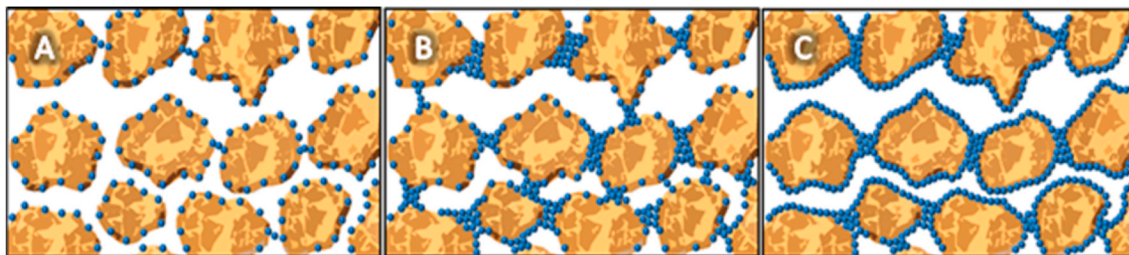


Fig. 12. Depiction of the mechanistic model of the retention of nanoparticles in sandstones. The retention process occurs in three distinct stages: A: static deposition, B: plugging and C: entrainment (cleaning).

Table 7
Summary of flow parameters and injectivity decline percentage for all experiments.

Exp. No.	pH	Np Conc. ppm	Cumulative PV Injected	Reference Perm. (k_0)	Perm. after Np Injection	Injectivity decline/recovery
			PVI	Darcy	Darcy	%
CF-1	7.2	50	1113	2.59	1.93	25.5
CF-2	7.1	100	38594	2.62	1.23	53.0
CF-2a	7.1	100	4111	2.62	1.29	-2.2
CF-3	7.4	50	37708	2.97	1.87	37.0
CF-3a	7.4	100	12346	2.97	1.79	2.7
CF-4	7.3	100	35549	3.21	2.23	31.0
CF-5	9.6	100	576	2.87	0.44	85.0
CF-6	4.0	100	428	2.75	1.20	56.5
CF-6a	7.3	100	4640	2.75	1.64	-16.0
CF-7 ^a	6.8	50	1782	3.24	0.26	92.0

^a Fractured core with iron ions.

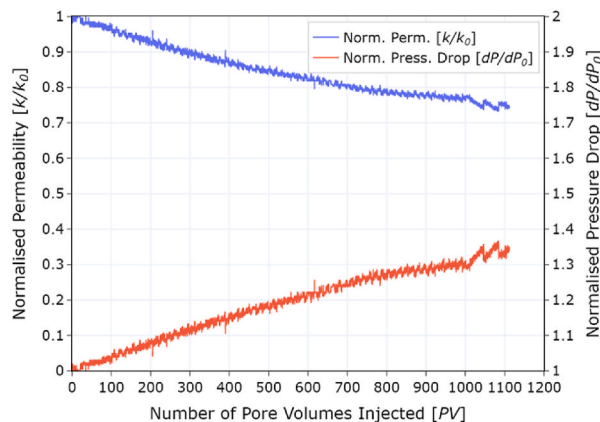
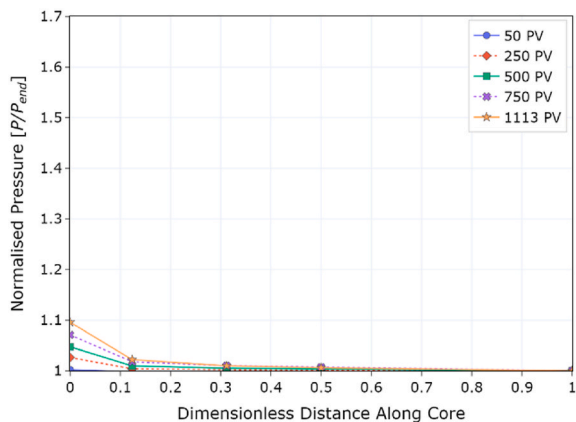


Fig. 13. CF1, left: Norm. pressure along the core at different PVs; right: Norm. permeability and pressure drop versus PVI.

number of PV with higher particle concentration. The section of the plug between the first two pressure gauges sees about 10 times more brine with higher nanoparticle concentration than the rest of the core (which sees a filtered suspension already). Therefore, the damage can be expected to be higher close to the inlet and lower downstream. In terms of injectivity, Fig. 13 (right) shows an almost linear decline in injectivity which is misleading as the long-term trend cannot be captured with this relatively low number of PV injected. This test demonstrates that correctly capturing the long-term trend requires a significantly larger volume to be injected when dealing with nanoparticles. Hence, the other core floods (CF-2 to CF-4) were run for a significantly longer time with higher flow rates. The oscillations in the pressure drop profile (Fig. 13, left) are caused by the frequent sampling at the inlet up to 1000 PV, followed by less frequent sampling.

3.2.2.2. Effects of nanoparticle concentration. In experiment CF-2, the nanoparticle concentration was kept at 100 ppm, the reference permeability was $k_0 = 2.62$ Darcy, and the flow rate was increased to 141 ml/min (which also provided more PVI within a limited time). This led to more than 38500 PV injected and we were able to capture the complete trend as oppose to CF-1. The results of this test are reported earlier in section 3.2.1.1 and Fig. 9. In CF-2a, the core holder was turned around to swap the inlet with the outlet for a reverse flow and further 4000 PV were injected. This resulted in a very limited permeability recovery of 2.2% of k_0 . This shows that once the stabilization plateau is reached, no further net nanoparticles retention occurs, and nanoparticles that were loosely retained during the CF-2 got released by reversing the flow in CF-2a. This supports the idea that the decline can be attributed to internal filtration rather than face plugging.

Core flood CF-3 tests the impact of lower nanoparticle concentration. The test starts with a concentration of 50 ppm up to about 38000 PV injected. Normalized pressure along the core shown in Fig. 14 (left) and injectivity decline shown in Fig. 14 (right) shows similar trends as CF-2 but less pronounced because of the lower nanoparticle concentration (and slightly higher k_0). This experiment was further extended into CF-3a where concentration was increased to 100 ppm as per Fig. 14 (right). This resulted in a limited additional decline of about 2.7% of k_0 . A possible explanation is that during CF-3, a “layer” of negatively charged nanoparticles got deposited which prevented further capture of particles.

3.2.2.3. Effect of permeability. The fourth core flood CF-4 tests the impact of higher permeability as well as the reproducibility of the results obtained in the CF-2 test as shown in Fig. 15. Hence, the nanoparticle concentration is 100 ppm and the reference permeability k_0 is 3.2D versus 2.62D of CF-2. The relative pressure build-up is significantly lower 1.2 (versus 1.65 for CF-2), which translates to an overall injectivity decline of 0.7 compared to 0.47 for CF-2. This test already gives some evidence on the expected impact of nanoparticles in lower permeability rock.

The core floods of the first set showed no visual EFC formation at the injection face at the end of tests as shown in Fig. 16. Hence, the injectivity decline is caused only via a deep filtration, consistent with a good propagation of the nanoparticles.

3.2.2.4. Effect of pH. Fig. 17 (left) shows the results for CF-5 (pH = 9.6) and CF-6 (pH = 4) aimed at investigating the impact of pH on the size of the nanoparticles and the resulting impact on injectivity. Compared to

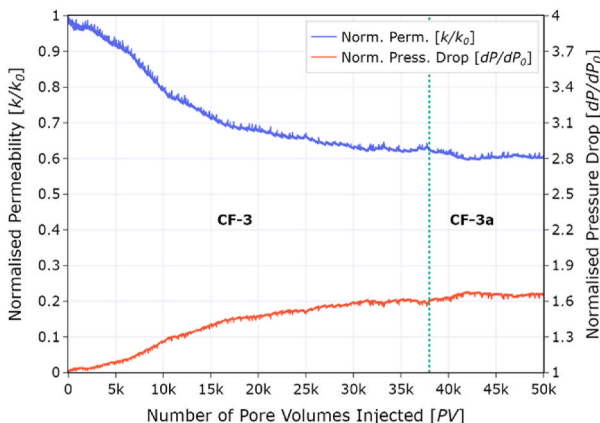
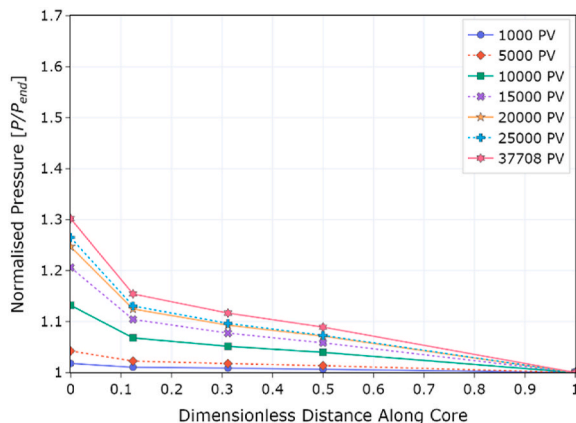


Fig. 14. CF-3, Left: Norm. pressure along the core at different PVs. Right: Norm. permeability and pressure drop over PVI.

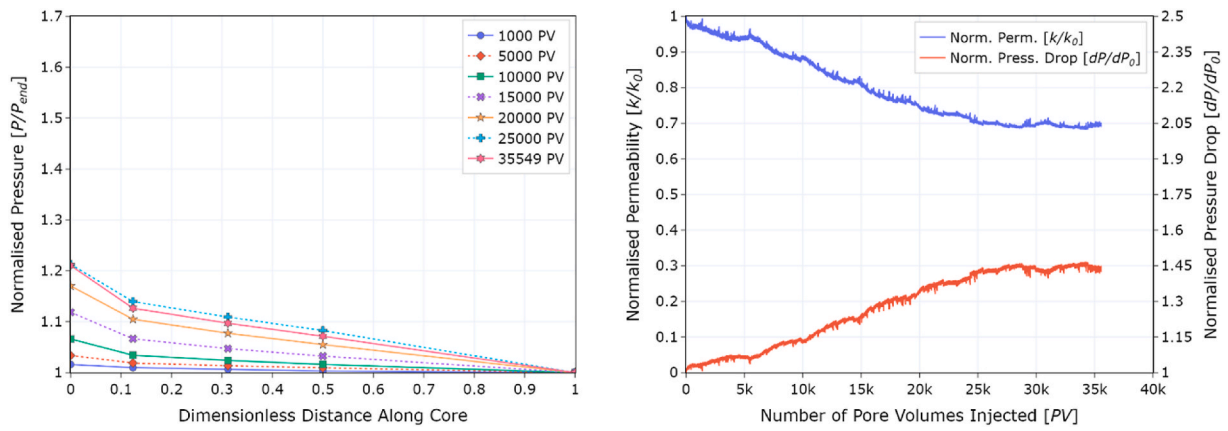


Fig. 15. CF-4, Left: Norm. pressure along the core at different PVs. Right: Norm. permeability and pressure drop over PVI.

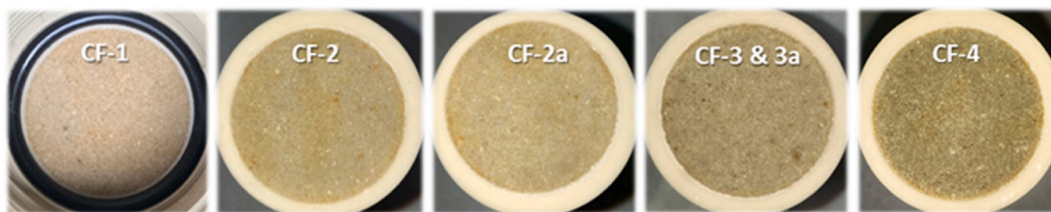


Fig. 16. Photos of the injection face of the core plugs post core flooding showing no external filter cake.

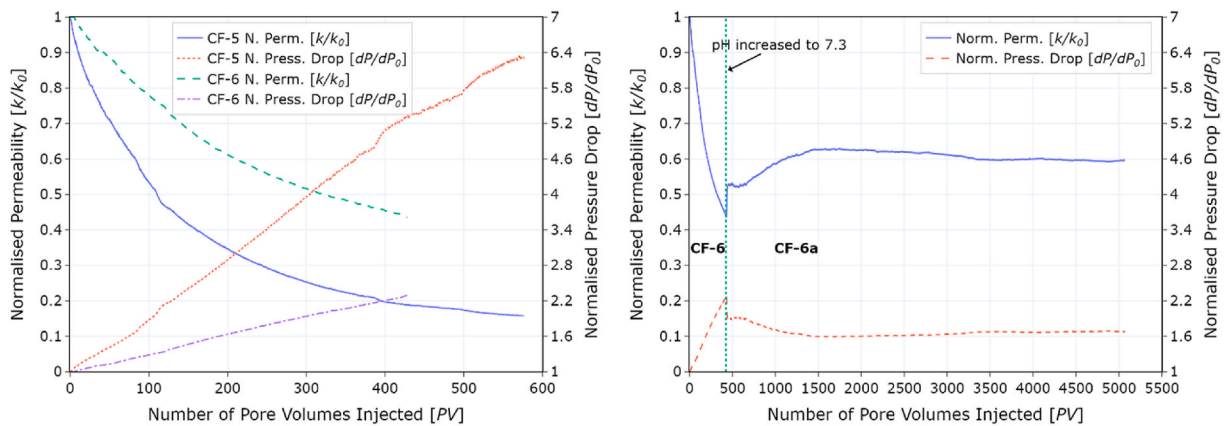


Fig. 17. Norm. permeability and pressure drop profiles. Left: CF-5 & 6, right: CF-6 & 6a.

CF-2 ($pH = 7.1$), the rate of decline is dramatically more severe. This suggests a different retention process where the formation of external filter cake (EFC) is dominantly responsible for injectivity decline. This was confirmed by the post-mortem as a stable EFC was observed at the

core inlet as per Fig. 18. Optical microscopy shows clearly a thick 1 mm EFC with a number of wormlike structures, which seemingly carried most of the flow. Comparing the permeability decline of CF-5 ($k/k_0 = 0.45$) and CF-6 ($k/k_0 = 0.2$) after 400 PVI, the difference is unlikely

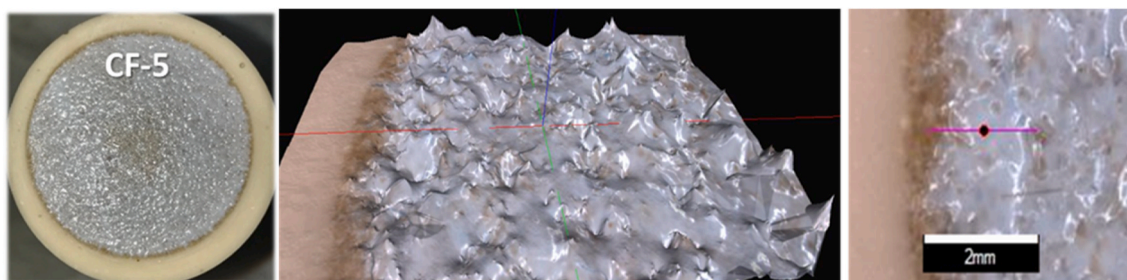


Fig. 18. EFC observed in CF-5. Left: picture of the inlet showing the EFC. Right: zoom showing the thickness of the EFC (~1 mm).

solely due to the difference in the reference permeability which is only 4%, i.e. within the error margin of the experiments. Following (Lawson et al., 2016; Peksa et al., 2015), a possible explanation of the higher rate of decline of permeability at high pH is the destabilization of clays and possibly the dissolution of the cementing compounds such as oxide minerals and calcites, leading to fines migration. CF-6 was further extended into CF-6a by injection of higher pH suspension (going from 4.0 to 7.3) as per Fig. 17 (right). This led to a recovery of about 16% of the reference permeability k_0 . The higher pH suspension dissolved the EFC, with zeta potential of nanoparticles becoming strongly negative, hence dispersing the nanoparticles which then get retained by the core.

3.2.2.5. Effect of iron ions ($Fe^{2+/3+}$). CF-7 tested the potential effect of corrosion material (iron) on the nanoparticle solution injectivity. Post-mortem CT scans of the core revealed the presence of a fracture along the flow direction as per Fig. 19 (left). Despite the high confining stress (25 Bar) applied during the core flood, some contribution of the fracture to the flow was expected. However, a drastic injectivity decline was observed as per Fig. 20. The injectivity decline was more severe than the other core floods. To explain this behaviour, we propose that the hydration of oxidized iron washer (Fig. 19, right) released iron ions ($Fe^{2+/3+}$) into solution, and they acted as a cross-linker between negatively charged nanoparticles. The aggregates thus formed caused the unexpected severe injectivity decline. To validate this hypothesis, bulk tests were conducted by preparing four samples using 0.1 M iron sulphate hepta-hydrate and 0.1 M iron chloride tetra-hydrate dissolved in the same nanoparticle suspension used in CF-7 as shown in Fig. 21.

The iron ions significantly reduced the pH of the suspension and iron oxide was formed. The measurements of the average hydrodynamic size and zeta potential confirmed that the injection nanoparticle solution was not stable due to the presence of iron oxide and dispersed particles were an order of magnitude bigger (μm size) than silica nanoparticles as shown in Table 8.

3.3. Nanoparticles transport model and simulations

3.3.1. Governing equations

We consider the flow of a suspension of nanoparticles with a concentration $c(x, t)$ (kg/m^3), and we denote $\sigma(x, t)$ (kg/m^3) the concentration of retained particles. Note that whereas c and σ have the same units, the former refers to the bulk volume of water, while the latter to the bulk volume of porous media. This might differ from the usage adopted by others in the literature. The total volume of solid can be expressed as

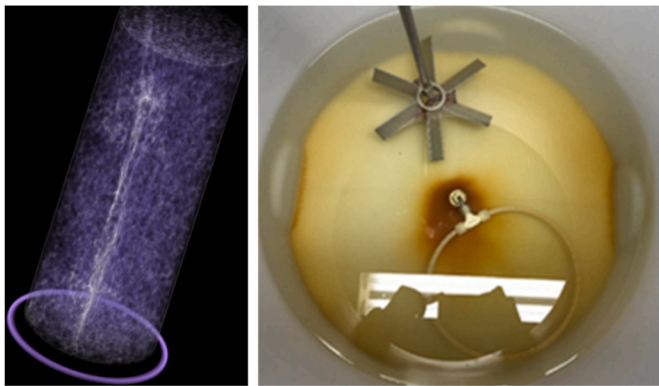


Fig. 19. CF-7 test - left: CT scan showing fracture along the core. Right: photo showing rust formation in the injection reservoir, the propeller to maintain nanoparticles in suspension with the inflow intake circular tube to ensure an optimal sampling of the suspension in terms of nanoparticle concentration.

$$V_{solid} = V(1 - \varphi_0) + V_{np} = V \left(1 - \varphi_0 + \frac{\sigma}{\rho_{np}} \right) \quad (1)$$

where V is the total volume of the porous medium, φ_0 is the initial porosity, V_{np} is the volume of the nanoparticles and $\rho_{np} = 2.2 \text{ g/cm}^3$ the nanoparticles effective density reported by the supplier. The change in porosity due to nanoparticles deposition/retention is therefore given by:

$$\varphi = \varphi_0 - \frac{\sigma}{\rho_{np}} \quad (2)$$

Many studies reported in the literature assume that retained concentration is rather small so that the change in porosity can be neglected (e.g. (Buret et al., 2010; Klov, 2000; Hower et al., 1972; Herzig et al., 1970) among others). Here, this assumption is relaxed to account properly for the effect of the decrease in porosity and ensuing the increase in local velocity on nanoparticle entrainment as discussed later. Therefore, we consider a continuum macroscopic model for the transport of nanoparticles in porous media accounting for their retention. We refer the reader to (Herzig et al., 1970) review paper and to (Civan, 2015) for a more detailed discussion of the microscopic filtration mechanics. After estimating the dispersion coefficient (molecular and hydrodynamic) and given the very high number of PVs injected in our experiments, dispersion is deemed not relevant. Based on mass conservation and retention kinetics (Khatib, 1994; Bennion et al., 2001; Klov, 2000; Civan, 2015; Iwasaki, 1937), the 1D corresponding governing equations can be written:

$$\begin{cases} \partial_t(\varphi c) + \partial_x(uc) = -\partial_t \sigma \\ \partial_t \sigma = \alpha \varphi c + \lambda uc - \psi(|v| - v_c)^+ \sigma \end{cases} \quad (3)$$

where Darcy's velocity u is given by $u = -(k/\mu)\partial_x p$. The third term, with the "+" sign, represents the entrainment when the norm of local velocity v becomes higher than the critical value v_c with an efficiency coefficient ψ . This critical value can also be interpreted in terms of shearing force threshold required to mobilize a particle (Herzig et al., 1970). The coefficient $\alpha = \alpha(x)$ and $\lambda = \lambda(x, \sigma)$ describe respectively the surface deposition (e.g. particle settling under gravity) and mechanical retention. In this work, we assume that mechanical trapping occurs only after a certain level of deposition σ_c has been reached. Hence, $\lambda(x, \sigma)$ can be expressed as:

$$\lambda(x, \sigma) = \begin{cases} \lambda(x) & \text{if } \sigma(x) > \sigma_c \\ 0 & \text{if } 0 < \sigma(x) \leq \sigma_c \end{cases} \quad (4)$$

This mechanical trapping coefficient $\lambda(x)$ expresses the likelihood that nanoparticles are captured by the porous medium, which increases with the specific area of the filter. Hence, as permeability decreases the specific surface increases and therefore the probability of particle capture increases. Therefore, we used the following functional form for λ :

$$\lambda(x, \sigma) = \lambda(K(x), \sigma) \sim \frac{\lambda^*(\sigma_c)}{\sqrt{\frac{k(x, \sigma)}{k(x, 0)}}} \quad (5)$$

where λ^* remains an empirical parameter, which captures the effects of mineralogy, solvent and nanoparticles interaction via their respective electrostatic forces. As deposition modifies the porosity, the local interstitial velocity is therefore modified as $v(t, x) = \frac{u}{\varphi(t, x)}$. Last, the permeability $k(x, \sigma)$ is updated using a simple permeability reduction model (Sharma et al., 2000) $k(x, \sigma)/k(x, 0) = \frac{1}{1 + \beta \sigma(x)}$, where $k(x, 0)$ is the reference permeability and β is an empirical parameter representing the impact of the deposition on the permeability reduction. In our history matching of the experiments, this parameter was not eventually required ($\beta = 1$). Initially, the core plug is assumed free of nanoparticles and deposits. At the injection face, the core is flooded with a homogeneous suspension of nanoparticle of concentration c_{inj} , hence:

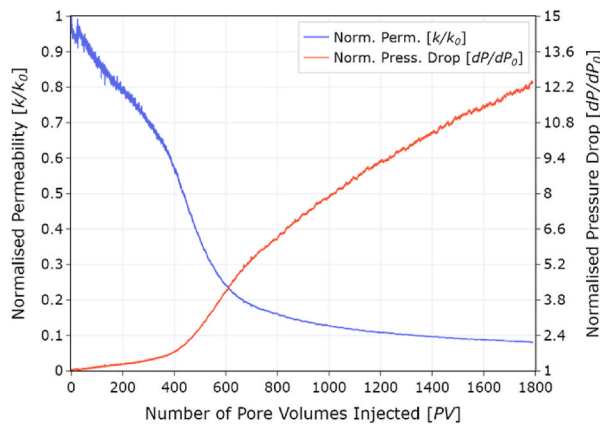
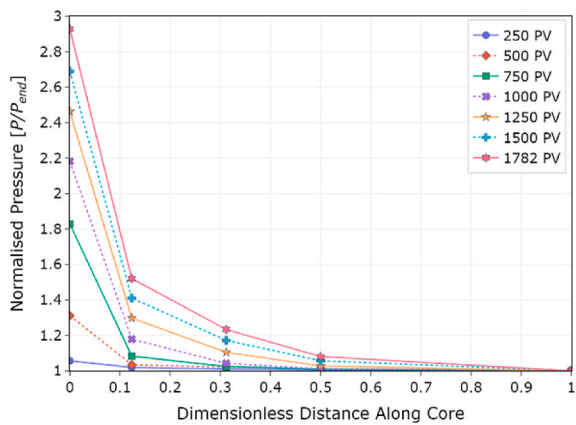


Fig. 20. CF-7 - Left: Norm. pressure along the core at different PVs. Right: Norm. permeability and pressure profiles.

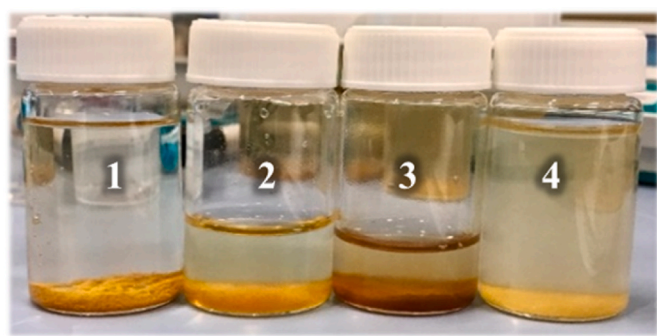


Fig. 21. Iron solutions: four samples made with the suspension used in the CF-7 core flood to which iron salts were added, showing clear iron oxide precipitate.

Table 8

Average hydrodynamic diameter and zeta potential measurements for samples containing iron salts (see Fig. 21 for the sample label).

S. No.	Sample Containing	Size	Zeta Ptnl.
		d, μm	mV
1	Iron sulphate hepta-hydrate (0.1 M Fe ⁺²)	16	+0.1
2	Iron sulphate hepta-hydrate (0.1 M Fe ⁺²) [0.45 μm filter]	1.3	+2.1
3	Iron chloride tetra-hydrate (0.1 M Fe ⁺²) [0.45 μm filter]	0.3	+11.9
4	Iron chloride tetra-hydrate (0.1 M Fe ⁺²)	8	+6.3

$$c(x, t = 0) = 0, \quad \sigma(x, t = 0) = 0, \quad c(0, t) = c_{inj} \quad (6)$$

In total, this model has a priori 6 parameters: α , λ , σ_c , v_c , ψ and β . However, these parameters may not be all independent or may even be redundant. Note that at equilibrium, the deposit rate is zero ($\partial_t \sigma = 0$) and the corresponding deposit σ_e and porosity ϕ_e satisfy the following quadratic equation:

$$\alpha c_0 \phi_e^2 + (\lambda u c_{inj} + \psi v_c \sigma_e) \phi_e - \psi u \sigma_e = 0 \quad (7)$$

Using (2), σ_e and ϕ_e can be determined in terms of the four model parameters α , λ , v_c , ψ to check if stabilization of the decline can be reached. Depending on the flow conditions, achieving an equilibrium requires the set of parameters to be within some specific range. This will be illustrated in the next section.

3.3.2. Comparing the transport model with the experiments

Equation (3) was solved implicitly on a grid size of 20 ($\Delta x = 0.85$ cm)

and timestep of 0.5 s to ensure numerical stability and convergence of the solution. Trials with an explicit scheme for (3) proved to be very unstable (first order scheme). Porosity and velocity update were done explicitly after the computation of σ . We use data from core floods CF-2, 3 and 4 to validate the model and interpret the different stages of the injectivity decline as summarized in Fig. 22. Three regions labelled A, B and C can be distinguished: region A corresponds to static deposition (α) with a low injectivity decline, region B corresponds to a more pronounced plugging (λ , σ_c) which ends when entrainment of the nanoparticles picks up (ψ , v_c) to eventually come to stabilizing in region C.

The combination of the model parameters matching a core flood experiment is inherently non-unique. To partial address this drawback, the matching of the model to the experiments was done region by region, starting with region A, then region B and finishing with region C. After obtaining the static deposition parameter α (slope of the decline in region A), the plugging (λ , σ_c) parameters were determined by matching the onset of the change in slope (σ_c) and the early slope (λ) of the decline in region B. To finalize the matching exercise, the entrainment (ψ , v_c) parts was determined by adjusting the critical velocity (v_c) and coefficient (ψ) to capture the onset of the stabilised plateau and its level in region C. The damage parameter β was fixed to unity for all the three core plugs indicating that this parameter was redundant.

Fig. 23 shows the pressure data (symbols) and the corresponding permeability decline for the three core floods CF-2 – CF-4 along with the model matching results (solid lines). The model clearly captures the different stages of the injectivity decline discussed earlier. The match is

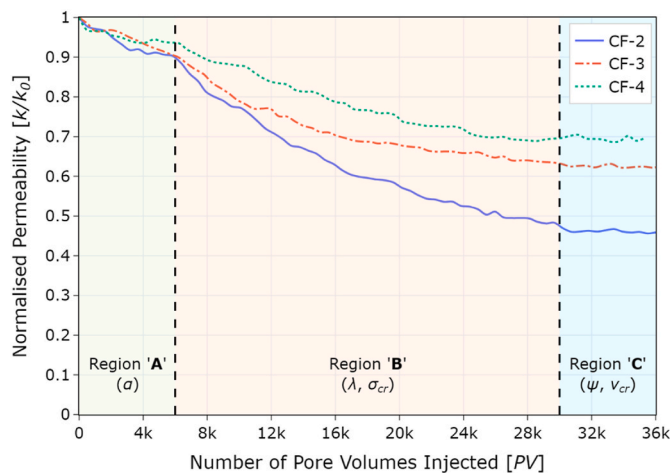


Fig. 22. Injectivity decline versus pore volumes injected for CF-2, 3 and 4 with the three distinctive decline regions. Horizontal axis is in thousands of PV injected.

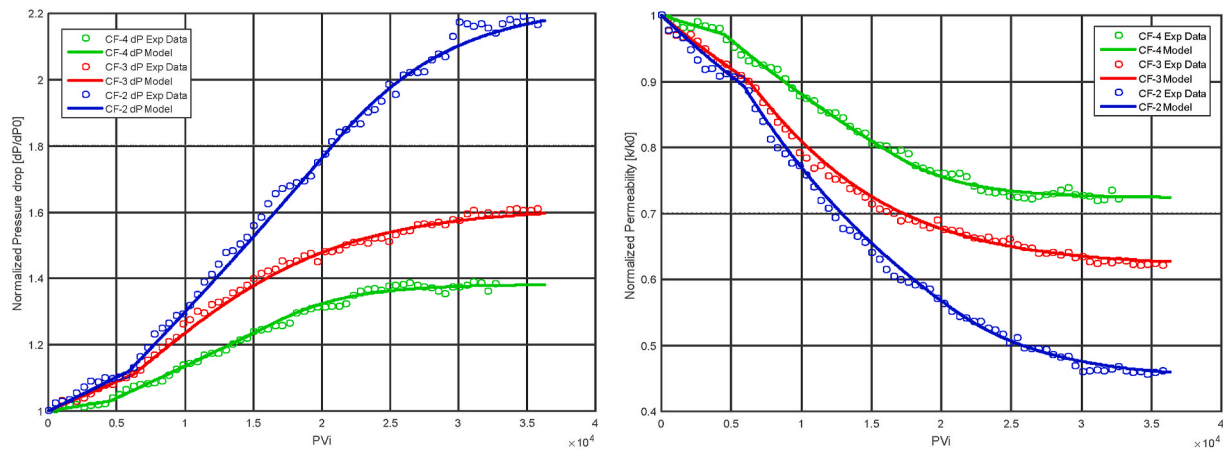


Fig. 23. Normalized pressure profiles CF-2, 3 and 4 core flood (left) and corresponding normalized permeability declines (right). Circles: experimental data; solid line: model matching. Note that horizontal axis is in 10 000 PVI.

very good as confirmed by the RMS (root mean square) values below 1%. The model parameters corresponding to the matching of each experiment are given in Table 9. The sensitivity to the critical entrainment velocity v_c comes from the fact that this critical velocity is very close to the interstitial velocity generated by the imposed flow rate of 141 ml/min, which is $V_0 = \frac{Q}{A\phi_0} \sim 8.224 \text{ E-3 m/s}$ for the three core floods. This means that entrainment is already happening with the imposed flow rate, and therefore does not require much extra deposition to be effective. The highest permeability core CF-4 ($k_0 = 3.21\text{D}$) shows a lower pressure drop increase as expected with a lower value of static α and plugging λ parameters.

As mentioned earlier, the value of the deposit at equilibrium σ_e can be formally computed from the model parameters using (7) to check further the consistency of the results. With the parameter values given in Table 9, the equilibrium deposits have been computed and reported in Table 10. The relatively small difference between the values obtained by solving (2) and (7) shows that the decline was close to equilibrium at the end of the experiments, with CF-4 showing a closer match. The amount of deposit at the equilibrium is consistent with the permeability range, whereby more retention is expected in lower permeability rock (CF-2) and therefore a more significant impact on the injectivity. These equations can also be used to investigate the impact of the model parameters on the equilibrium without the need of simulation.

The smoothness of the solution does not capture the real physics suggested by the data fluctuations. Although variability in the data is expected as part of the experimental measurements, the balance between the plugging and entrainment is expected to generate real physical fluctuations as intermittence. It is expected that plugging periods will be followed by cleaning (entrainment) periods and vice versa as particles plug some flow paths inducing local pressure build-up and local velocities leading to clean-up. A more detailed modelling and experimental work to explore this behaviour will be part of the follow-up investigations.

Table 9
Model parameters used for matching core flood experiments.

Exp. No.	K_0	c_0	α	σ_e	$\lambda^*(\sigma_e)$	v_c/V_0	ψ	RMS Error
	Darcy	ppm	s^{-1}	kg/m^3	m^{-1}	[--]	m^{-1}	
CF-2	2.62	100	4.60e-5	1.20e-1	5.40e-3	1.00160	0.30	0.78%
CF-3	2.97	50	8.00e-5	1.10e-1	7.50e-3	1.00034	0.40	0.67%
CF-4	3.21	100	1.20e-5	0.30e-1	3.10e-3	1.00054	0.80	0.68%

Table 10
Comparison of equilibrium deposit values for the three core floods CF-2, CF-3 and CF-4.

Exp. No.	σ_e [kg/m ³]		
	End simulation	Equation (11) and Table 9	Error
CF-2	1.1784	1.1586	-1.71%
CF-3	0.5959	0.5828	-2.25%
CF-4	0.4261	0.4243	-0.40%

4. Summary and conclusions

Injectivity decline in high permeability rock induced by ultra-filtered water injection was investigated. Silica nanoparticles suspension was used as a proxy to ultra-filtered water. A special care in testing the conditions for good nanoparticle dispersion was taken before conducting corefloods. Long-term injectivity decline were conducted only with salinity and pH range where a very good nanoparticle dispersion was obtained. Other core flood tests were also conducted to confirm the expected impact on injectivity when salinity, pH or iron ions lead to nanoparticles agglomeration. High volume of nanoparticle solutions (>40 000 PVs) were injected which allowed us to reach a stable injection region. Based on the results obtained, the following conclusions could be drawn:

- The stability of the nanoparticles as dispersed suspension is very sensitive to the brine salinity and pH and iron ions. For values of salinity, pH and iron ions outside a specific window, nanoparticles form bigger aggregates resulting in visual external filter cake formation, and a significant injectivity decline.
- When the salinity and pH of the brine are kept within the optimal range and free of iron ions, nanoparticles propagate through the full

core plug with some retention. This retention results in injectivity decline following three clear stages: surface deposition, plugging and entrainment. Once stability in injectivity decline is reached, increase in nanoparticle concentration or flow reversal would have a limited effect on that stability plateau.

- For iron ions free solutions, external filter formed by nanoparticles because of pH or salinity could be removed by injecting brine with pH and salinity within the optimal range.
- The presence of (positive) iron ions results in drastic injectivity decline, even though the core plug had a fracture along the flow direction. However, because of the high confining stress the contribution of the fracture to the flow might have been limited. The strong interaction between the nanoparticles and the iron ions shows that making water clean at some location in the injection system may not suffice to ensure good injectivity. Corrosion products along the injection lines may be detrimental to the high water quality produced upstream.
- The nanoparticles transport is interpreted using a deep bed filtration (DBF) model which includes the three major retention mechanisms (surface deposition, plugging and entrainment) and is found to be in very good agreement with experimental results. The entrainment part is key to capture the injectivity stability plateau.

This work shows that ultra-filtered water still results in significant injectivity decline even in very permeable rock. It is expected that this injectivity decline will worsen in low permeability rock. However, compared to publications on micron-sized particles, the propagation (and production) of nanoparticles shows that an injection decline stability can be reached, whereas micron-sized particles lead mostly to a filter-cake formation with drastic damage to injectivity. In particular, we can expect that in the case where the leak-off area is big enough (e.g. fractured wells) sustained injectivity with ultra-filtered water may be achieved with limited fracture growth. Another important consequence of this work is that technologies based on nanoparticles for EOR might

need revisiting using more realistic injection volume to ensure that potential injectivity impairment due to nanoparticles is included. Further work on the stability of dispersion of nanoparticles with times, via aging, would complete further the understanding and provide more insight on the robustness of such particles as they propagates into harsher subsurface environment. Intermittence in injectivity due to the balancing between the plugging and cleaning process could be further investigated as a potential source of vibration/noise in the system.

Author contributions

The first author initiated the paper write-up and generated the first draft. He also supervised the experiments and the experimental design along with the numerical interpretation. The second author made the literature review, conducted the experiments, generated all the data, and contributed to the writing. The third author supervised the work, reviewed the manuscript, and contributed to improving the paper and presentation of this work.

Declaration of competing interest

The authors declare that they have no known competing financial interests or personal relationships that could have appeared to influence the work reported in this paper.

Acknowledgements

The authors acknowledge Marc Friebe from TU Delft laboratory for his help in the experimental work as well as Marcelis Fons and Hilbert van der Linde, both from Shell, for their support in the CT-scans of the core and measurement of the nanoparticle sizes. We are grateful to Paul van den Hoek for fruitful discussions. We thank Shell Global Solutions International for the sponsoring and the permission to publish this work.

Nomenclature

DBF	Deep bed filtration
DLS	Dynamic light scattering
DSW	Diluted sea water
EFC	External filter-cake
IFC	Internal filter-cake
MIP	Mercury Intrusion Porosimetry
PEEK	Poly etherether ketone
ppm	Parts per million
PSD	Pore size distribution
SEM	Scanning electron microscopy
TEM	Transmission electron microscopy
TSS	Total suspended solids
XRD	X-ray diffraction
XRF	X-ray fluorescence
A	Cross-sectional area
c	Concentration of nanoparticles
c_{inj}	Concentration of nanoparticles at in injection suspension
σ	Concentration of retained particles (deposition)
σ_c	Critical concentration of retained particles
σ_e	Deposition at equilibrium
ρ_{np}	Effective density of nanoparticles
φ_0	Initial porosity
φ_e	Porosity at equilibrium
u	Darcy's velocity
k	Permeability
μ	viscosity
v	Local velocity

v_c	Critical velocity
ψ	Efficiency coefficient
α	Surface deposition coefficient (particle settling under gravity)
λ	Mechanical retention coefficient
Q	Flux
V	Volume of porous medium
V_{solid}	Volume of solids
V_{np}	Volume of nanoparticles

References

- Abrams, A., 1977. Mud design to minimize rock impairment due to particle invasion. *J. Petrol. Technol.* 29, 586–592.
- F. A. H. Al-Abduwani, Ph.D Doctoral dissertation, Delft University of Technology, 2005.
- F. Al-Abduwani, R. Farajzadeh, P. Bedrikovetsky, W. van den Broek and P. Currie, 2004.
- Alaskar, M., Ames, M., Connor, S., Liu, C., Cui, Y., Li, K., Horne, R., 2012. Nanoparticle and microparticle flow in porous and fractured media—an experimental study. *SPE J.* 17, 1160–1171.
- J. Altoe F, P. Bedrikovetsky, A. Siqueira, A. Souza and F. Shecaira, 2004.
- Barkman, J.H., Davidson, D.H., 1972. Measuring water quality and predicting well impairment. *J. Petrol. Technol.* 24, 865–873.
- Bedrikovetsky, P., Marchesin, D., Shecaira, F., Souza, A., Milanez, P., Rezende, E., 2001. Characterisation of deep bed filtration system from laboratory pressure drop measurements. *J. Petrol. Sci. Eng.* 32, 167–177.
- Bennion, D.B., Thomas, F., Imer, D., Ma, T., Schulmeister, B., 2001. Water quality considerations resulting in the impaired injectivity of water injection and disposal wells. *J. Can. Petrol. Technol.* 40.
- Buret, S., Nabzar, L., Jada, A., 2010. Water quality and well injectivity: do residual oil-in-water emulsions matter. *SPE J.* 15, 557–568.
- F. Civan, 2007.
- Civan, F., 2015. *Reservoir Formation Damage*. Gulf Professional Publishing.
- Clark, C., Harto, C., Sullivan, J., Wang, M., 2010. *Water Use in the Development and Operation of Geothermal Power Plants*. Argonne National Lab.(ANL), Argonne, IL (United States).
- Coradin, T., Eglin, D., Livage, J., 2004. The silicomolybdc acid spectrophotometric method and its application to silicate/biopolymer interaction studies. *Spectroscopy* 18, 567–576.
- L. Costier, P. J. van den Hoek, C. J. Davidson, M. Ding, J. van den Berg and R. Hofland, 2009.
- Dautriat, J., Gland, N., Guelard, J., Dimanov, A., Raphanel, J.L., 2009. Axial and radial permeability evolutions of compressed sandstones: end effects and shear-band induced permeability anisotropy. *Pure Appl. Geophys.* 166, 1037–1061.
- A. H. De Zwart, Doctoral dissertation, Delft University of Technology, 2007.
- Dordzie, G., Dejam, M., 2021. Enhanced oil recovery from fractured carbonate reservoirs using nanoparticles with low salinity water and surfactant: A review on experimental and simulation studies. *Adv. Colloid Interface Sci.* 293, 102449. <https://doi.org/10.1016/j.cis.2021.102449>.
- Elimelech, M., Gregory, J., Jia, X., 2013. *Particle Deposition and Aggregation: Measurement, Modelling and Simulation*. Butterworth-Heinemann.
- Eylander, J., 1988. Suspended solids specifications for water injection from coreflood tests. *SPE Reservoir Eng.* 3, 1287–1294.
- M. Halisch, E. Vogt, C. Müller, A. Cano-Odena, D. Pattyn, P. Hellebaut and K. van der Kamp, 2013.
- Herzig, J., Leclerc, D., Goff, P.L., 1970. Flow of suspensions through porous media—application to deep filtration. *Ind. Eng. Chem.* 62, 8–35.
- T. Hofsaess and W. Kleinitz, 2003.
- Hower, W., Lasater, R., Mihram, R., 1972. *Compatibility of Injection Fluids with Reservoir Components*.
- K. Ives, 1969.
- Iwasaki, T., 1937. Some notes on sand filtration. *J. Am. Water Works Assoc.* 29, 1591–1597.
- Kalantariasl, Ph.D Doctoral dissertation, University of Adelaide, 2015.
- Z. Khatib, 1994.
- T. Klov, Dr. Ing Doctoral thesis, Norwegian University of Science and Technology, 2000.
- Kottsova, A.K., Yegane, M.M., Tchistiakov, A.A., Zitha, P.L., 2021. Effect of electrostatic interaction on the retention and remobilization of colloidal particles in porous media. *Colloids Surf. A Physicochem. Eng. Asp.* 617, 126371.
- Lawson, R., Gresham, T., Richardson, I., Siega, F., 2016. S. Addison and N. Zealand.
- Liu, X., Civan, F., 1996. Formation damage and filter cake buildup in laboratory core tests: modeling and model-assisted analysis. *SPE Form. Eval.* 11, 26–30.
- Maloney, D., Honarpour, M., Brinkmeyer, A., 1990. *The Effects of Rock Characteristics on Relative Permeability*. National Inst. for Petroleum and Energy Research, Bartlesville, OK (USA).
- A. Murtaza, M.Sc. Master thesis, Delft University of Technology, 2017.
- L. Nabzar, J.-P. Coste and G. Chauveteau, 1997.
- S. O. Olayiwola, MDejam, *Comprehensive experimental study on the effect of silica nanoparticles on the oil recovery during alternating injection with low salinity water and surfactant into carbonate reservoirs*. *J. Mol. Liq.*, 325: 115178.
- Peksa, A.E., Wolf, K.-H.A., Zitha, P.L., 2015. Bentheimer sandstone revisited for experimental purposes. *Mar. Petrol. Geol.* 67, 701–719.
- Ryan, J.N., Elimelech, M., 1996. Colloid mobilization and transport in groundwater. *Colloids Surf. A Physicochem. Eng. Asp.* 107, 1–56.
- Sharma, M.M., Pang, S., Wennberg, K., Morgenthaler, L., 2000. Injectivity decline in water-injection wells: an offshore gulf of Mexico case study. *SPE Prod. Facil.* 15, 6–13.
- Van Baaren, J., Vos, M., Heller, H., 1990. *Selection of Outcrop Samples*. Delft University of Technology.
- Veil, J.A., Clark, C.E., 2011. Produced-water-volume estimates and management practices. *SPE Prod. Oper.* 26, 234–239.
- Vilks, P., Miller, H., Doern, D., 1991. Natural colloids and suspended particles in the Whiteshell Research Area, Manitoba, Canada, and their potential effect on radiocolloid formation. *Appl. Geochem.* 6, 565–574.
- Watson, S., 2017. *How Geothermal Energy Works*. <https://science.howstuffworks.com/environmental/energy/geothermal-energy.htm>. (Accessed 20 October 2017).
- Willhite, G.P., 1986. *Waterflooding*. *Soc. Petrol. Eng.* 326pp.
- T. Yi, A. Fadili, M. N. Ibrahim and B. S. Al-Matar, 2009.